Research Article

Electrical transport in lead-free Na$_{0.5}$Bi$_{0.5}$TiO$_3$ ceramics

J. SUCHANICZ^a, K. KLUCZEWSKA-CHMIELARZ^{a,*}, D. SITKO^b, G. JAGŁO^a

^{a}*Institute of Technology, Pedagogical University, ul. Podchorazych 2, 30-084 Krakow, Poland*
^{b}*Institute of Physics, Pedagogical University, ul. Podchorazych 2, 30-084 Krakow, Poland*

Abstract: Lead-free Na$_{0.5}$Bi$_{0.5}$TiO$_3$ (NBT) ceramics were prepared via a conventional oxide-mixed sintering route and their electrical transport properties were investigated. Direct current (DC, σ_{DC}) and alternating current (AC, σ_{AC}) electrical conductivity values, polarization current (first measurements) and depolarization current, current–voltage (I–U) characteristics (first measurements), and the Seebeck coefficient (α) were determined under various conditions. The mechanism of depolarization and the electrical conductivity phenomena observed for the investigated samples were found to be typical. For low voltages, the I–U characteristics were in good agreement with Ohm's law; for higher voltages, the observed dependences were I–U^2, I–U^4, and then I–U^6. The low-frequency σ_{AC} followed the formula σ_{AC}–ω^s (ω is the angular frequency and s is the frequency exponent). The exponent s was equal to 0.18–0.77 and 0.73–0.99 in the low- and high-frequency regions, respectively, and decreased with temperature increasing. It was shown that conduction mechanisms involved the hopping of charge carriers at low temperatures, small polarons at intermediate temperatures, and oxygen vacancies at high temperatures. Based on AC conductivity data, the density of states at the Fermi-level, and the minimum hopping length were estimated. Electrical conduction was found to undergo p–n–p transitions with increasing temperature. These transitions occurred at depolarization temperature T_d, 280 ℃, and temperature of the maximum of electric permittivity T_m is as typical of NBT materials.

Keywords: Na$_{0.5}$Bi$_{0.5}$TiO$_3$ (NBT) ceramics; electrical properties; Seebeck coefficient; impedance spectroscopy

1 Introduction

Lead zirconate titanate (PZT) and PZT-based ceramics have been widely utilized in various electromechanical devices [1,2]. Nevertheless, ceramics with lead content present a considerable environmental hazard during the manufacturing process, usage, and subsequent recycling. Lead-free materials have therefore attracted attention as potential replacements for lead-based ceramics. In

this context, ferroelectric materials based on Na$_{0.5}$Bi$_{0.5}$TiO$_3$ (NBT) [3–7], K$_{0.5}$Bi$_{0.5}$TiO$_3$ (KBT) [8,9], and Na$_{0.5}$K$_{0.5}$NbO$_3$ (NKN) [10,11] have been studied extensively. Recent investigations made by Hu's group have shown NBT-based ceramics to be high-performance materials suitable for application in next-generation energy storage capacitors [12–14].

NBT crystalizes with a perovskite structure and exhibits a sequence of transformations from the high-temperature cubic phase ($Pm\overline{3}m$) to the tetragonal one ($P4bm$) at 540–520 ℃, and then to the rhombohedral phase ($R3c$) at about 260 ℃ [15–18]. The tetragonal

* Corresponding author.
E-mail: kamila.kluczewska-chmielarz@up.krakow.pl

and rhombohedral phases appear to coexist in a wide temperature range of 350–200 ℃ [15–19]. The tetragonal phase is non-polar (or weakly polar) and the rhombohedral phase is ferroelectric. The temperature dependence of electric permittivity of NBT has a maximum $T_m \approx 320$ ℃, related to relaxation processes which should originate from both electrical and mechanical interactions between the polar and non-polar phases [20], and a local anomaly at the so-called depolarization temperature $T_d \approx 190$ ℃, which shows weak relaxation behavior [19]. Transmission electron microscopic (TEM) investigations suggest that the rhombohedral-to-tetragonal phase transformation may involve an intermediate modulated orthorhombic (*Pnma*) phase [21]. Neutron scattering measurements indicate that at high temperatures (far above T_m), unstable polar regions arise [22]. The correlation radius of these regions increases with decreasing temperature and below 280 ℃ they are stable. They act as centers for the nucleation of the ferroelectric phase, which occurs below a temperature of about 200 ℃.

In ferroelectrics, the study of electrical transport characteristics (particularly the order and nature of electrical conductivity) is extremely important, since they affect other associated properties such as piezoelectricity, pyroelectricity, and poling conditions for these materials. However, electrical transport in NBT materials is a subject that has rarely been investigated [23–25]. There are no data on the polarization current or *I–U* characteristics, and only a few data of the Seebeck coefficient (α) [26] for this material.

In this paper, investigations of the charging currents, depolarization currents, *I–U* characteristics, electrical conductivity, and α of NBT ceramics are presented. The study provides deep insight into the charge transport mechanism in NBT.

2 Experimental

NBT ceramic samples were prepared via the conventional solid-state reaction method [3,5]. High-purity Na_2CO_3 (99.99%), Bi_2O_3 (99.99%), and TiO_2 (99.9%) reagents were used. Hygroscopic Na_2CO_3 was first dried at 200 ℃ for 1 h in order to remove the absorbed water. A mixture of the powders in stoichiometric ratios was homogenized in an agate mortar for 4 h, uniaxially pressed into pellets at 120 MPa, and calcined at 700 ℃/1.5 h, 750 ℃/1 h, and 800 ℃/2 h in air. After

the third calcination, the product was crushed into fine powders, pressed, and subsequently sintered at 1100 ℃/1 h and 1160 ℃/1.5 h. These conditions are very similar to those applied by other groups [27–29]. The formation and quality of the compounds were verified using X-ray diffraction (XRD) analysis. The relative density of the specimens was measured using the immersion method based on Archimedes' principle and was found to be greater than 95% of the theoretical density (which was assumed to be 5.998 g·cm^{-3} [30]). This implies that the conditions selected for the preparation of the specimens were appropriate.

Direct current (DC, σ_{DC}) electrical conductivity was measured over the temperature range from room temperature (RT) to 600 ℃ using a Keithley 6517A electrometer, whereas AC electrical conductivity alternating current (AC, σ_{AC}) and impedance spectroscopy measurements were performed over the frequency and temperature ranges from 100 Hz to 2 MHz and from RT to 600 ℃, respectively, for silver electrode samples, using a GW 821LCR meter.

The polarization/depolarization currents and *I–U* characteristics were measured using the Keithley 6517A electrometer. These measurements require precise temperature stabilization to avoid the influence of pyrocurrents. Stabilization to within 0.001 ℃ was achieved. In the case of polarization currents, the current flowing from the sample under an applied electric field (5, 15, and 20 kV/cm) was measured. When measuring depolarization current, the sample was polarized at 5, 15, and 25 kV/cm for 1 or 2 h at the chosen temperatures. It was then short-circuited and the depolarization current flowing from the sample was measured.

The α was measured in the temperature range of 50–370 ℃. The sample was placed in a thermostat between heated silver blocks, which made it possible to create a temperature gradient inside the sample (for more details see Ref. [26]). After the sample reached the selected temperature, the temperatures of the electrodes were controlled in such a way as to achieve a 10 ℃ difference (ΔT) between them. The values of the α were determined from the slope of the linear dependences between the electromotive force (E) and ΔT.

3 Results and discussion

To characterize the obtained samples, X-ray, microstructural,

and electric permittivity investigations were performed.

The obtained samples have a pure perovskite structure (Fig. 1(a)). The splitting of $(110)_c$ and $(111)_c$ peaks indicates rhombohedral symmetry. However, a small shoulder on the left side of the $(200)_c$ peak (indicated by the arrow) suggests a more likely mixed-phase nature of NBT (e.g., regions of the tetragonal phase are presented in the rhombohedral matrix [3]). The weak reflection below the $(111)_c$ peak (indicated by the arrow) is the evidence of the presence of space group $R3c$.

Figure 1(b) shows the microstructure of polished and chemically etched surfaces and energy disperse spectroscopy (EDS) analysis of NBT ceramics. As can be seen, grains of different sizes are densely packed and are homogeneously distributed throughout the sample's surface. No secondary phase or unreacted starting reagents were observed in the sample. A small number of scattered pores are observed, which indicates that the 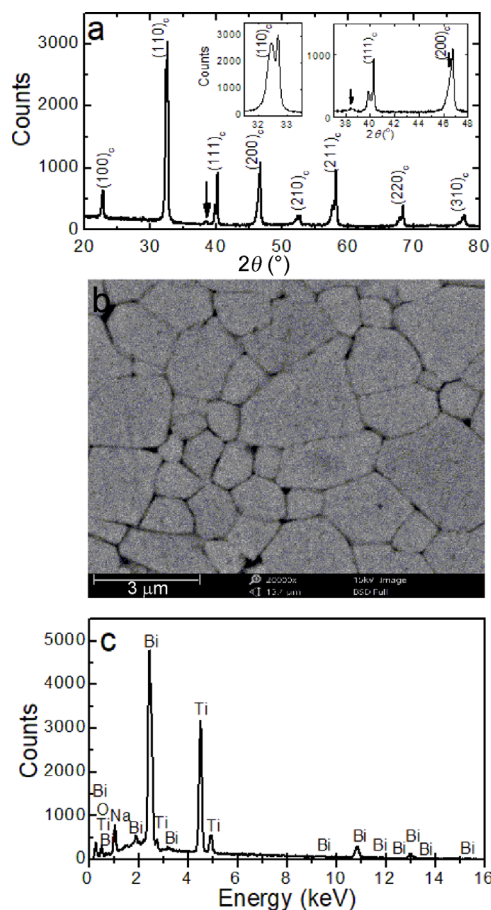samples exhibit a certain degree of porosity. The average grain size, determined by counting the number of grains along the diagonal, is about 1.7 μm. EDS analysis indicated that the distribution of all elements throughout the grains was homogeneous and that the composition within experimental error was very close to the stoichiometric one.

Two anomalies are visible in the temperature dependence of electric permittivity of the investigated NBT ceramics: One at a lower temperature (at $T_d \approx$ 190 ℃) and the other at a higher one $T_m \approx$ 318 ℃ (Fig. 2). The first anomaly—at the so-called depolarization temperature (T_d)—is related to the disappearance of the long-range ferroelectric phase, and the second one—at T_m—is associated with the maximum of electric permittivity. Large thermal hysteresis can be the evidence of a first-order phase transition and can reflect internal stress caused mainly by the coexistence of the rhombohedral and tetragonal phases (inset (a) of Fig. 2). Note that this hysteresis appears below T_m, which indicates that the material is metastable in this temperature range. The anomaly at T_d indicated relaxor-like features (inset (b) in Fig. 2). A broad anomaly in the temperature dependence of the dielectric
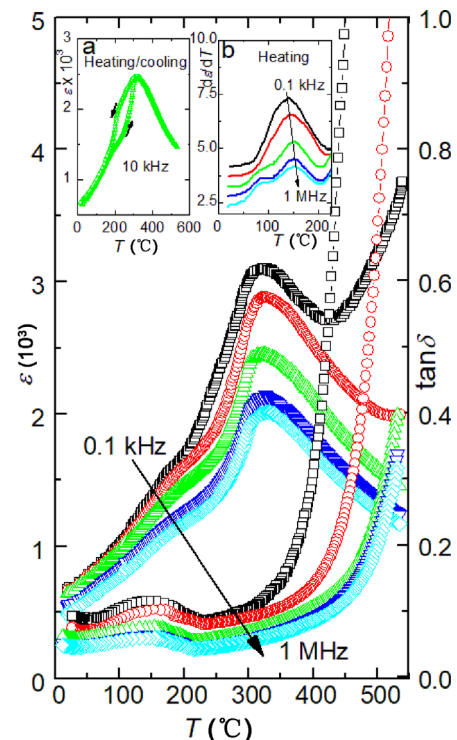

Fig. 1 (a) XRD pattern recorded for NBT ceramics at RT, (b) SEM image of the polished and chemically etched surface, and (c) EDS analysis of the NBT ceramics.

Fig. 2 Temperature/frequency evolution of electric permittivity (ε) and dielectric loss (tanδ) of NBT ceramics. Inset (a) shows the temperature dependence of ε upon heating/cooling (f = 10 kHz). Inset (b) shows the first derivative of ε in a narrow temperature range.

loss tan$\delta(T)$ was observed near T_d (Fig. 2).

The *I–U* characteristics, which were plotted for current values measured 10, 100, and 1000 s after the electric field had been applied, and under steady-state time (t_s) current conditions, are shown in Fig. 3. As can be seen, Ohm's law was obeyed at low electric field strength and depends on temperature. However, for the strongest field, the dependence $I–U^2$ is followed. Finally, four slopes of $I(U)$ plots are clearly visible: $I–U$, $I–U^2$, $I–U^4$, and $I–U^6$ (see the steady-state current conditions presented in Fig. 3(d)). The slopes were obtained based on linear fits of the $I(U)$ plots. According to the space-charge-limited current (SCLC) theory [31], strongly defected surfaces of grains provide a source of deep trap states, in which the trapped charge carriers are excited by the applied electric field and thermal energy. Below the onset electric field, ohmic current flows. For higher electric fields, the current characteristics start to follow the tendency $I–U^{\alpha}$, where $\alpha = 1.2–2$ [31]. The concentration of excess injected charge carriers in the case of a high electric field is greater than that at thermal equilibrium. When temperature increases, the concentration of equilibrium charges increases, which can lead to shifting conditions for the appearance of SCLC into higher electric fields. The results shown in Fig. 3(d) clearly confirm this tendency. When the electric field reaches a trap-filled limit value, the current increases more rapidly and the *I–U* characteristics

depend on trap distribution of the form $I–U^n$ ($n = 2, 4, 6, \ldots$), as in the case of the presented results.

Figure 4 presents the time dependence of the depolarization current of NBT ceramics. As can be seen, each curve features two straight lines with different slopes, separated by an intermediate interval [32]. As temperature increases, the time of this cross-over shifts towards lower values. The depolarization current (I_d) follows an inverse function:

$$I_d = At^{-p} \tag{1}$$

where A is a constant dependent on temperature and t is the polarization time. The power index p depends on field strength, polarization time, and temperature [32].

The activation energy determined from depolarization current values increases from 0.29 ± 0.02 eV, for the temperature range from RT to 190 ℃ (the range for which the ferroelectric phase is observed), to 0.48 ± 0.02 eV, for the temperature range of 190–220 ℃ (the range for which the rhombohedral/tetragonal phases are observed) [32]. This is the result of the appearance of new energy levels with higher activation energy, mainly due to changes in the structure of the material. The processes that take place during depolarization are related to the processes that are characteristic of the electrical conduction.

In general, two components of the depolarization current may be distinguished: (i) The current related to polarization, which disappears due to the reorientation of domains (ferroelectric component) and (ii) the current
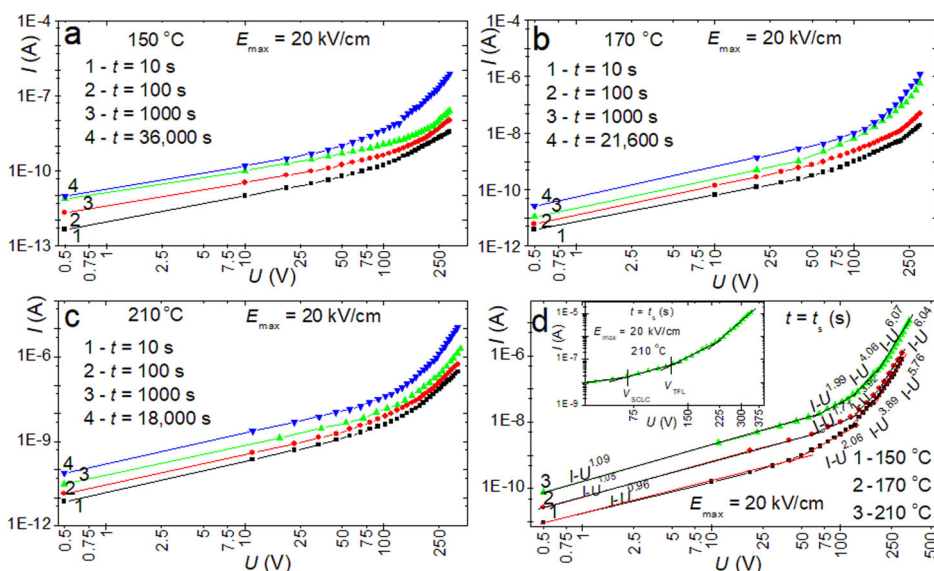
Fig. 3 *I–U* characteristics of NBT ceramics were measured several times (a–c) after an electric field of varying strength had been applied, and (d) under steady-state current conditions. In the inset in (d), the voltage at which the transition from ohmic behavior to space-charge limited current occurs (V_{SCLC}) and the trap-filled limit voltages (V_{TFL}) at temperature 210 ℃ are indicated.
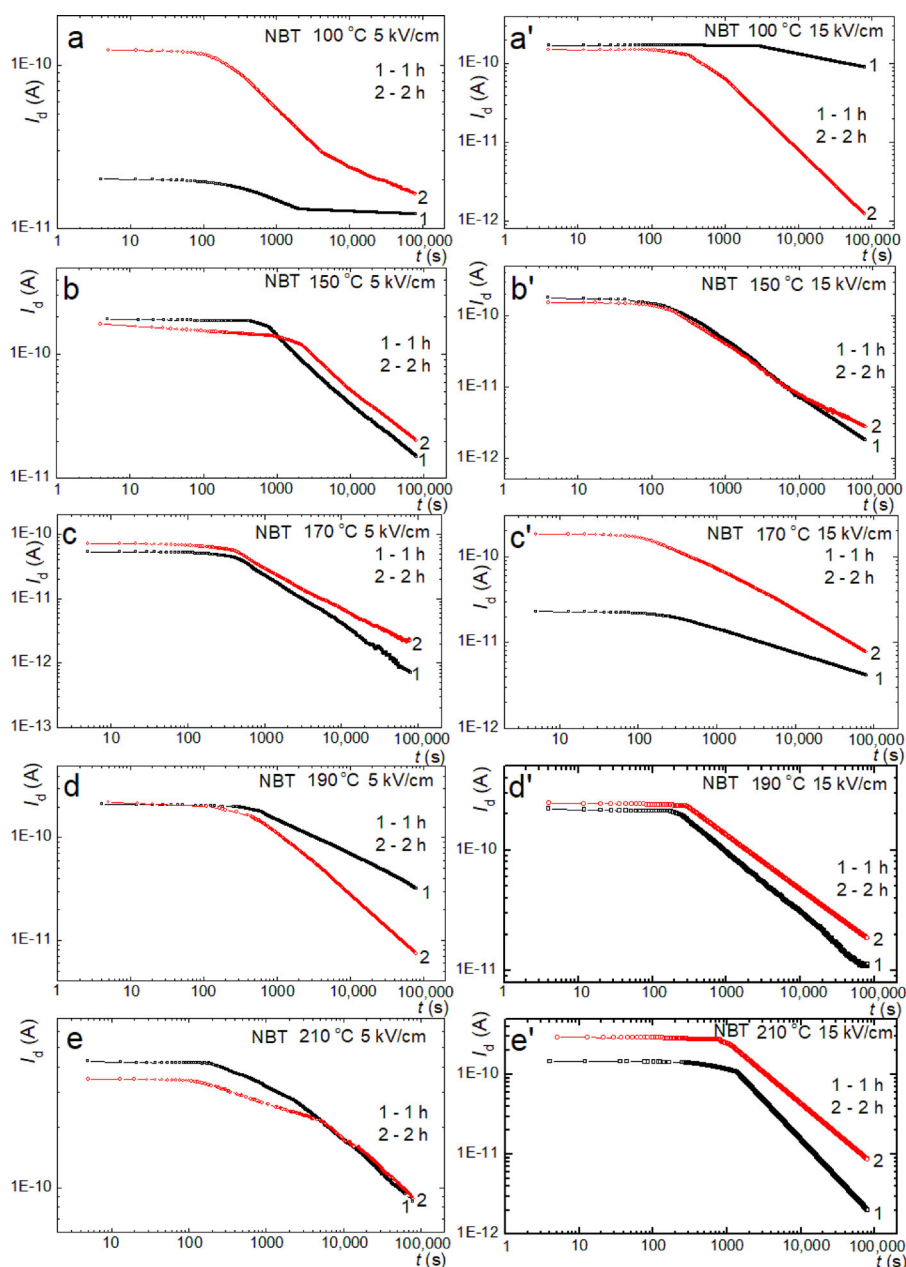
Fig. 4 Depolarization currents of NBT ceramics measured after applying an electric field of either (a–e) 5 kV/cm or (a′–e′) 15 kV/cm for 1 and 2 h and at different temperatures. Note that both axes utilize a log scale.

resulting from the decay of other kinds of polarization, e.g., dipole and ionic (non-ferroelectric component). Since there are correlations between certain types of polarization, there is a connection between ferroelectric and non-ferroelectric currents. Localized states (potential centers) of different origin may occur in NBT. Free charges and charges injected from electrodes (in high electric fields) may be trapped by these centers, which may include domain walls, point defects, or dislocations. In NBT, point defects associated with oxygen deficiencies—among others—may occur, which leads

to the subsequent appearance of long-range potential centers. After the electric field is deactivated, the domains randomize and charges trapped by domain walls and point defects, and dislocations are released. This means that the sample undergoes depolarization, and the depolarization current flows through it [33]. The migration of charge carriers between potential centers can be an important transport mechanism for polarization/depolarization/electrical conduction processes.

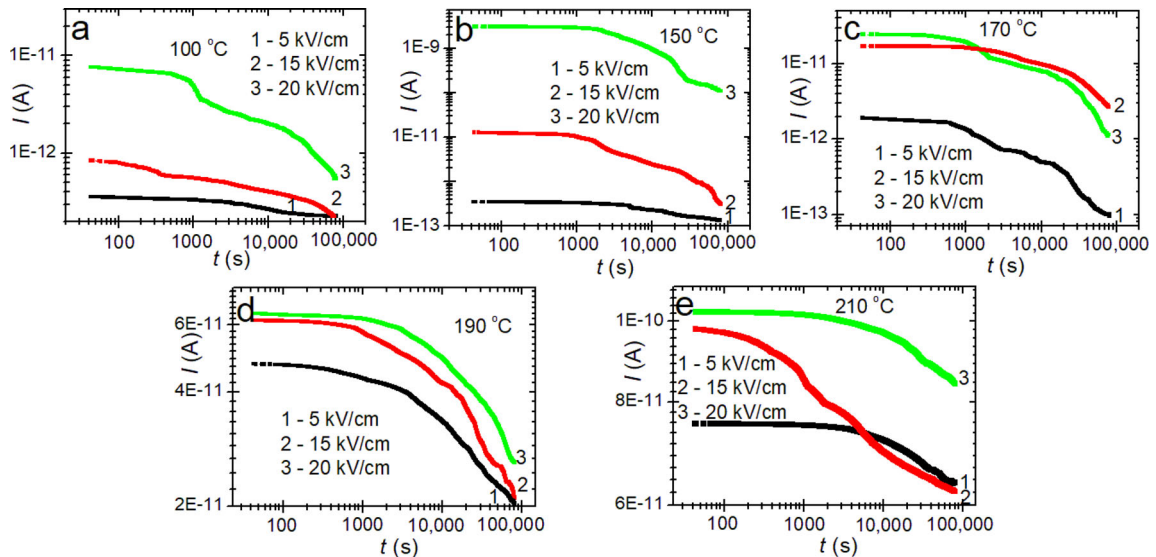Figure 5 shows the polarization current at several

Fig. 5 Charging currents of NBT ceramics for applied electric fields of 5, 15, and 20 kV/cm at different temperatures. Note that both axes utilize a log scale.

temperatures and for applied electric fields of 5, 15, and 20 kV/cm. As can be seen, the time required for polarization saturation depends on the strength of the polarizing electric field and the temperature. In a low polarizing field, polarization reaches saturation after a long time (65,000 s). In general, the electric field applied to a ferroelectric material causes a change in the domain configuration and the displacement of free/localized charge carriers. The changes in domain configuration result from the movement of domains/ domain walls and the nucleation of new domains, with the rates of these two processes being dependent on electric field strength and temperature. In weak electric fields, the polarization process takes a long time [34]. As free charges undergo localization due to the trapping and screening of polarization, their number decreases with time and the sample relaxes towards equilibrium. In this state, only DC conductivity current flows through the sample (Fig. 6). Before the state of equilibrium is reached, and immediately after the application of the electric field, several transient currents are observed [35]. Examples include the space-charge-limited transient current, which decays rather rapidly. As the transient current associated with the movement of the domains/domain walls decays rather slowly (particularly for low fields), the total transient current for longer time is determined by the rate of this movement.

In perovskite ferroelectric materials, oxygen vacancies are considered mobile carriers, and potential centers associated with them may be observed. The ionization
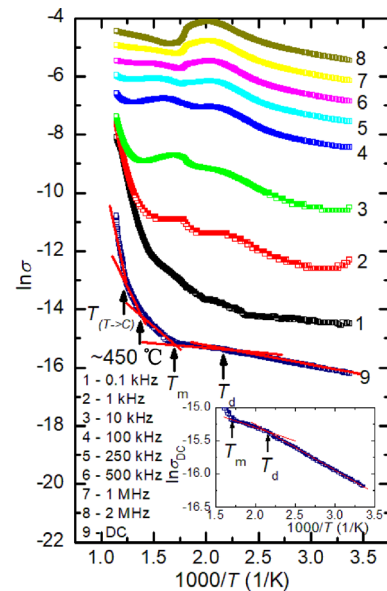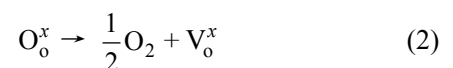

Fig. 6 Electrical conductivity of the investigated NBT ceramics as a function of $1000/T$ for various frequencies. The temperature $T_{(T \to C)}$ denotes the change from tetragonal to cubic symmetry. Inset: magnified section showing two linear dependences in the following ranges of low temperatures: (1) RT–T_d and (2) T_d–T_m.
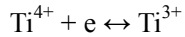
of these vacancies creates conduction electrons, a process which is represented by the Kröger–Vink notation [36]:

$$O_o^x \; \to \; \frac{1}{2}O_2 + V_o^x \tag{2}$$

$$V_o^x \; \to \; V^{\bullet} + e' \tag{3}$$

$$V_o^{\bullet} \leftrightarrow V_o^{\bullet\bullet} + e' \tag{4}$$

Excess electrons and oxygen vacancies are thus formed during reduction:

$$O_o^x \rightarrow \frac{1}{2}O_2 + V_o^{**} + 2e \tag{5}$$
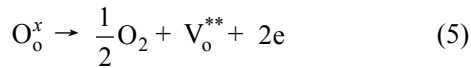
They may bond to Ti^{4+} in the form:

$$Ti^{4+} + e \leftrightarrow Ti^{3+}$$

(e.g., hopping of electrons between localization sites) (6)

Electrons trapped by Ti^{4+} ions or oxygen vacancies may be thermally activated, enhancing conduction. Doubly charged oxygen vacancies are considered to be the most mobile charges in perovskites and to play an important role in the conduction process [37]. In NBT, the volatilization of A-site elements during the sintering process results in the generation of oxygen vacancies, which compensate for negatively charged A-site vacancies.

Whilst DC conductivity requires the migration of carriers from one electrode to another, AC conductivity is connected with their short-range motion. The latter type of conductivity depends on temperature and the frequency of the electric field.

The plot representing $\ln\sigma$ as a function of $1000/T$ for various frequencies including σ_{DC} is shown in Fig. 6. As can be seen, electrical conductivity increases with temperature increasing, indicating the negative temperature coefficient of resistance (NTCR) of a semiconductor, with an anomaly at T_d and T_m. σ_{DC} increases with temperature increasing and the linear correlation between $\ln\sigma_{DC}$ and $1000/T$ in some temperature regions suggests the validity of the relation:

$$\sigma_{DC} = \sigma_0\exp(-E_c/k_BT) \tag{7}$$

where σ_0 is the pre-exponential factor and E_c, k_B, and T are the activation energy of conduction, Boltzmann's constant, and absolute temperature, respectively. A careful inspection of Fig. 6 reveals two linear parts of the $\ln\sigma_{DC}$ ($1000/T$) curve in the low-temperature range: from RT to about T_d and from T_d to about T_m. These two linear parts with two different activation energy values may be predominantly related to different scattering mechanisms in different temperature ranges (in the low-temperature region, a long-range rhombohedral ferroelectric state is observed; at higher temperatures, the rhombohedral and tetragonal phases coexist). This may be related to a certain change in the conduction mechanism at T_d. Finally, five linear parts of the curve for DC conductivity can be distinguished with five different activation energies: (i) *ca.* 0.06 eV for the range of the lowest temperatures, (ii) *ca.* 0.04 eV

in the temperature range from T_d to T_m, (iii) *ca.* 0.29 eV for the temperature range from T_m to 450 ℃, (iv) *ca.* 0.65 eV for the temperature range of 450–540 ℃, and (v) about 1.96 eV for the high-temperature range, i.e. 540–600 ℃ (Table 1). Thus, electrical conductivity measurements also showed the intermediate temperature of 450 ℃ to be significant aside from the well-known temperatures (540 ℃, T_m, and T_d). These activation energies are markedly lower than the optical energy gap of 3.2 eV [38], which is why electrical conduction in NBT may be said to be mediated by impurities. Since the activation energies calculated from electrical conductivity correspond to those obtained from depolarization current values, it can be concluded that both phenomena share the same underlying mechanism. The ion distribution in NBT is expected to be inhomogeneous, which causes a certain degree of disorder. In this case, charge carriers (electrons, polarons, holes, ions, etc.) can move between localized states. This movement is mainly caused by hopping, trapping/de-trapping, or excitation. The value of activation energy for the ferroelectric phase (0.06 eV) may be related to carrier hopping between localized sites (e.g., $Ti^{4+} + e \leftrightarrow Ti^{3+}$). The value of 0.04 eV may be associated with the small polarons created by the electron and/or hole-phonon interactions and is reinforced by lattice mismatch in the range in which the rhombohedral and tetragonal phases coexist. The values of 0.29, 0.65, and 1.96 eV suggest a possibility that conduction in the range of higher temperatures for ionic charge carriers may be mediated by oxygen vacancies (motion of first and/or second ionization oxygen vacancies). The increase in conductivity in this temperature range can be attributed to the increase in the concentration of ionized vacancies.

The increase of σ_{AC} with temperature increasing can be caused by the increased density and/or mobility of free carriers. In the low-frequency range, the electric field acts on charge carriers over a long period, which favors their increased localization. Since localized charge carriers are eliminated from further transport,

Table 1 Activation energy of the NBT ceramics for five temperature intervals

Temperature interval (℃)	Activation energy (eV)
RT–T_d	0.06
T_d–T_m	0.04
T_m–450	0.29
450–540	0.65
540–600	1.96

electrical conductivity decreases in this frequency interval (Fig. 6).

AC conductivity varies with frequency (Fig. 7), which may be associated with the existence of free as well as bound carriers. Conductivity increases with frequency, which leads to the conclusion that bound carriers play a predominant role in the conduction process in NBT. The increase in conductivity with frequency may be explained by the hopping of carriers between the trap levels situated in the energy gap, as expressed by the following law [39]:

$$\sigma_{AC} = A\omega^s \tag{8}$$

where *s* is the frequency exponent, which is a function of both frequency and temperature and generally ranges from 0 to 1. The exponent *s* was calculated from the slopes of the $\ln\sigma_{AC}$ vs. $\ln f$ dependence (Fig. 7). The *s* decreases with increasing temperature, which is predicted by the hopping model. AC conduction in NBT can therefore be concluded to be of the hopping type (e.g., the short-range translational-type hopping of charge carriers). This suggests that the conduction process is thermally activated. For the low-frequency range (up to about 10 kHz), *s* is in the range of 0.18–0.77. For the higher-frequency region, s ranges from 0.73 to 0.99. In both the low- and high-frequency regions, the value of *s* tends to unity at low temperatures, which is another indication that the conduction mechanism in NBT is of the hopping type. If *s* = 1, the interaction between neighboring dipoles is almost negligible (Debye behavior).
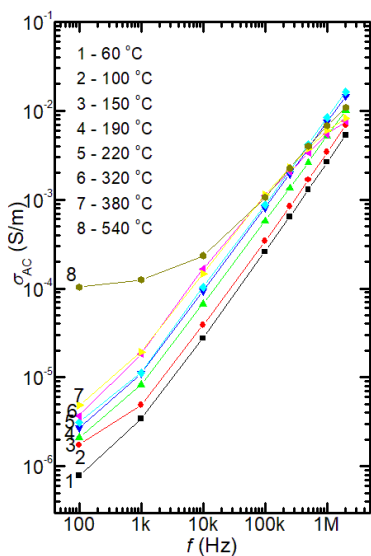
The temperature dependence of α is shown in Fig. 8. The fact that the α is almost completely independent of temperature in the low-temperature range up to about T_d is an indication that carrier mobility rather than carrier concentration is thermally activated in this temperature interval. Those are expected results for the hopping model. The positive value of α in this temperature (from RT to about 200 ℃) range indicates that p-type conductivity is predominant. The exposure of oxygen vacancies to an oxygen-containing environment during the cooling of the samples after the sintering process or during the annealing step creates holes (h$^\bullet$), leading to a p-type conduction behavior ($\frac{1}{2}O_2 + V_O^{\bullet\bullet} = O_O^x + 2h^\bullet$). These holes have higher mobility than oxygen vacancies. The α decreases with a further increase in temperature and at about 220 ℃ it changes sign from positive to negative and increases up to 235 ℃. This means that first carrier-mediated conduction (e.g., the excitation of minority carriers at high temperature) increases and that the conductivity mechanism changes to n-type. In the temperature from ~220 to 235 ℃, the carrier concentration decreases and/or their mobility increases. At about 310 ℃, α changes sign from negative to positive and slightly increases up to about 320 ℃ (near T_m), after which it starts to decrease. This dynamic temperature behavior of α, which indicates a change in the sign of carriers and their concentration/mobility, takes place in the wide temperature range in which the rhombohedral and tetragonal phases coexist. This behavior also allows to distinguish the temperatures T_d and T_m that are characteristics of NBT.
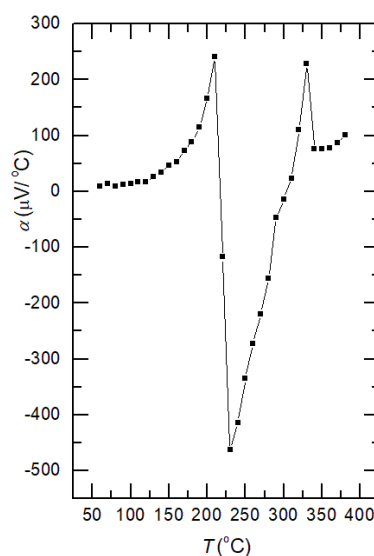

Fig. 7 σ_{AC} of NBT ceramics as a function of frequency at different temperatures.

Fig. 8 α of NBT ceramics as a function of temperature.

For perovskites (non-degenerate semiconductors), the α can be expressed using the following equation [40]:

$$\alpha = (k_B/e)\ln(N_c/n) \tag{9}$$

where N_c is the effective density of states in the conduction band, n is the carrier concentration, and e is the electronic charge. It was assumed that N_c for the transport level is temperature independent and is equal to the number of ionic sites per 1 cm^3 (1.56×10^{28} m^{-3} for NBT).

Electrical conductivity is given by the equation [41]:

$$\sigma = en\mu \tag{10}$$

where μ is the mobility of charge carriers and n is the carrier concentration. The values n and μ were calculated using Eqs. (9) and (10) and their temperature dependences are shown in Fig. 9. As can be seen, both n and μ increase with temperature increasing. The low value of the mobility of charge carriers also suggests that the hopping mechanism contributes significantly to electrical conduction [39,42].

Based on the obtained σ_{AC} values, the density of states at the Fermi-level ($N(E_f)$)[43] was calculated:

$$\sigma_{AC}(\omega) = \left(\frac{\pi}{3}\right)e^2\omega k_B T[N(E_f)^2]\alpha^{-5}[\ln(f_0/\omega)]^4 \tag{11}$$

where f_0 represents photon frequency (10^{13} Hz) and α is the localized wave function (10^{10} m^{-1}). Figure 10 shows the temperature dependence of $N(E_f)$ at different frequencies. In general, $N(E_f)$ increases with temperature increasing, while anomalies at temperatures roughly equal to T_d and T_m are clearly visible. As can be seen from the inset in Fig. 10, the frequency-related changes in $N(E_f)$ have a different character in the temperature range from RT to approximately T_d and in the temperature range above T_d. The high values of $N(E_f)$ indicate that hopping between pairs of sites is the predominant constituent of the charge transport in the investigated samples.

The minimum hopping length (R_{min}) was estimated using the following equation [44]:

$$R_{min} = 2e^2 / (\pi\varepsilon\varepsilon_0 W_m) \tag{12}$$

where W_m represents binding energy, which was estimated from the equation $s = 1 - (6k_B T/W_m)$. W_m is the energy required to remove charge carrier from one site and relocate it to another. It first increases up to a temperature roughly equal to T_m, and then decreases as temperature rises (Fig. 11(a)). R_{min} changes in the opposite manner. In addition, R_{min} is almost completely independent from the frequency at RT, which suggests that charge carrier transport proceeds along an infinite percolation path [45]. However, R_{min} increases with frequency at higher temperatures (above T_m), which suggests that in this range transport is mediated predominantly by hopping in the finite cluster [45].

SCLC are observed when electrodes in contact are capable of injecting electrons in the conduction band (E_c) or holes in the valence band of the material. At low external electric fields (voltages), the injection of excess charge carriers into the sample is weak, and Ohm's law is obeyed. However, in the case of a high external electric field, injection is far more pronounced. With increasing temperature, the range of electric field strength for which Ohm's law valid shifts towards higher values (Fig. 3(d) and Table 2). The voltage at which the transition from ohmic behavior to SCLC occurs, V_{SCLC} can be calculated using the following
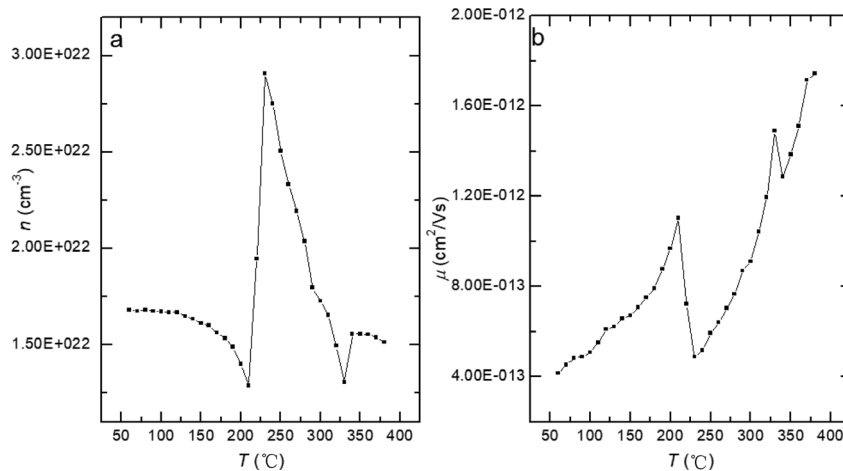

Fig. 9 Temperature dependence of (a) n and (b) μ in NBT ceramics.
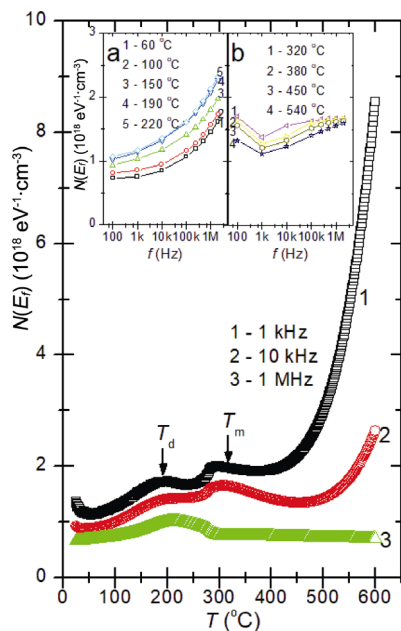
Fig. 10 Temperature dependence of the Fermi-level density of states ($N(E_f)$) of NBT ceramics at several frequencies. Insets (a) and (b) show the frequency dependence of $N(E_f)$ at different temperatures, which demonstrates the different characteristics of this dependence for the temperature ranges from RT to about T_d and above T_d.
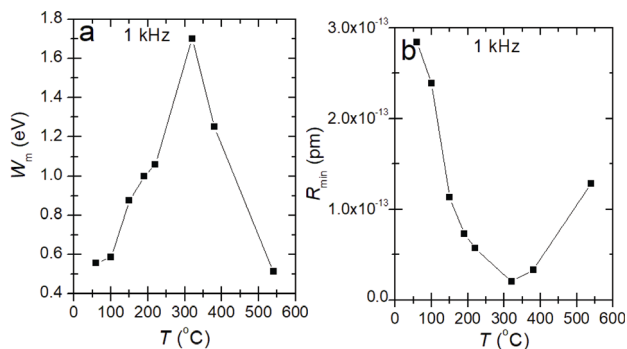

Fig. 11 (a) W_m of NBT ceramics at 1 kHz and (b) R_{min} of NBT ceramics at 1 kHz.

Table 2 V_{SCLC} and V_{TFL} values of the NBT ceramics at 150, 170, and 210 ℃

	150 ℃	170 ℃	210 ℃
V_{SCLC} (V)	40	60	68
V_{TFL} (V)	130	120	114

equation [46,47]:

$$V_{SCLC} = \frac{ed^2 n}{2\varepsilon\varepsilon_0 \theta} \quad (13)$$

where ε represents the electric permittivity of the material, n is the carrier concentration stands for the

density of free carriers at thermal equilibrium and θ is the coefficient which determines to what degree charge carrier undergoes trapping. The coefficient θ is equal to

$$\theta = \frac{n}{n_t} = \frac{N_c}{gN_t} \exp\left(\frac{E_t - E_c}{k_B T}\right) = \frac{N_c}{gN_t} \exp\left(\frac{-E_t}{k_B T}\right) \quad (14)$$

where n_t is the density of trapped carriers, N_c is the density of states in the conduction band, N_t is the density of traps, g represents the degradation coefficient ($g = 2$), and E_t is the trap energy level below the edge of E_c.

The electrical conductivity (σ) for materials that obey Ohm's law is given by Eq. (10). Finally, the relation for θ is as follows:

$$\theta = \frac{d^2\sigma}{2\varepsilon\varepsilon_0\mu V_{SCLC}} \quad (15)$$

The value of θ estimated from Eq. (15) is 4.84 × 10^{-4} and 1.74 × 10^{-4} at temperatures of 150 ℃ (below T_d) and 210 ℃ (above T_d), respectively. These values are consistent with those obtained for other perovskites [48–50].

When the strength of the electric field (voltage) applied to the sample is very high, the Fermi-level passes through the trap level and all traps become filled. In this case, the current flowing through the sample rapidly increases. The voltage at which this occurs is known as the V_{TFL}, and it is expressed as follows [46,47]:

$$V_{TFL} = \frac{ed^2 N_t}{2\varepsilon\varepsilon_0} \quad (16)$$

where the value of N_t was calculated from Eq. (16) and was then used as input for Eq. (14). The energy of trapping states (E_t) was thus obtained (Table 3).

The time of movement (diffusion) of charge carriers from one electrode to another can be estimated by taking the process of their trapping into account. Perovskite materials can contain anywhere from 10^{23} to 10^{25} m^{-3} oxygen vacancies, which are one type of trapping centers. The active cross-section (S) for charge carrier (electron) trapping by these vacancies is equal

Table 3 N_t and E_t below the edge of E_c and θ of the NBT ceramics at 150, 170, and 210 ℃

	150 ℃	170 ℃	210 ℃
N_t (m^{-3})	8.78 × 10^{20}	1.15 × 10^{21}	1.20 × 10^{21}
E_t (eV)	0.86	0.92	1.01
θ	4.84 × 10^{-4}	2.69 × 10^{-4}	1.74 × 10^{-4}

to 10^{-18} m^2 [51]. The mean free path for trapping is $\lambda = 1/(n{\cdot}S) = 10^{-5}$–$10^{-7}$ m. Thus, a charge carrier is trapped many times before crossing the path determined by the specimen's thickness.

The time of movement (diffusion) of charge carriers (electrons) (t) can be estimated from the following equation:

$$t = \frac{\tau d^2}{\lambda^2} \tag{17}$$

where τ is the relaxation time for which charges are held in a trap with depth E_t, and can be calculated as follows:

$$\frac{1}{\tau} = SN_c\upsilon\exp\left(\frac{-E_t}{k_BT}\right) \tag{18}$$

where υ represents the thermal velocity of charge.

For values of $d = 0.00017$ m, $\upsilon = 10^5$ m/s, $N_c = 1.56 \times 10^{28}$ m^{-3}, and $E_t = 0.86$, 0.92, and 1.01 eV for 150, 170, and 210 ℃, respectively, t values ranging from 10^{-7} to 10^{-3} s were obtained depending on the assumed number of defects. However, aside from oxygen vacancies, there are other trapping centers, which can increase the value of t.

Impedance spectroscopy is widely used as a standard characterization technique for many polycrystalline ferroelectric materials. The response of the system as a function of the perturbation frequency can provide insight into the internal behavior of dipolar structures. In addition, this method is a reliable tool for the optimization of the properties of dielectric materials and the procedure of their preparation.

The data in the complex plane can be represented in any of the four basic formalisms, namely complex impedance (Z^*), complex admittance (Y^*), complex permittivity (ε^*), and complex electric modulus (M^*). They are defined by the following equations [52,53]:

$$Z^* = Z' - jZ'' = 1/j\omega C_0\varepsilon^* \tag{19}$$

$$M^* = M' + jM'' = 1/\varepsilon^* = j\omega C_0 Z^* = \varepsilon'/(-j\varepsilon'') \tag{20}$$

$$Y^* = Y' + jY'' = j\omega C_0\varepsilon^* \tag{21}$$

$$\varepsilon^* = \varepsilon' - j\varepsilon'' \tag{22}$$

$$\tan\delta = \varepsilon''/\varepsilon' = M''/M' = Z'/Z'' = Y'/Y'' \tag{23}$$

$$M^* = M' + jM'' = \varepsilon'/(\varepsilon'^2 + \varepsilon''^2) - j\varepsilon''/(\varepsilon'^2 + \varepsilon''^2) \tag{24}$$

where $\omega = 2\pi f$ is the angular frequency, and Z', M', Y', ε' and Z'', M'', Y'', ε'' are the real and imaginary components of impedance, electrical modulus, admittance and permittivity, respectively.

Modulus spectroscopy plots are particularly useful for separating the spectral components of materials that exhibit similar resistance but different capacitances. The electrical modulus corresponds to the relaxation of the electric field in the material when the electric displacement remains constant, and represents the real dielectric relaxation process. It was originally introduced by Macedo *et al.* [52] to study space charge relaxation. M^* representation is now widely used when analyzing ionic conductivity [53].

The complex modulus spectra $M'' = f(M')$ at different temperatures are given in Fig. 12. The spectra are characterized by two semicircular arcs with a pattern that changes with increasing temperature. The intercept of the first semicircle with the real axis indicates the total capacitance contributed by the grain interior capacitance (on the high-frequency side), whereas the intercept of the second one indicates the total capacitance contributed by the grain boundary capacitance (on the low-frequency side). The shape of the curves undergoes a marked change as temperature increases. The observed changes suggest that the capacitance of the grain and grain boundary decreases with temperature increasing. This observation indicates that the electrical properties of this material are controlled by the temperature/ microstructure and this behavior might be explained by combined parallel and serial arrangement of grain interiors and boundaries.

The frequency dependence of the imaginary parts of the electrical modulus is shown in Fig. 13. Frequency response was examined in the range from 20 Hz to 2 MHz. In this frequency range, well-known electrical
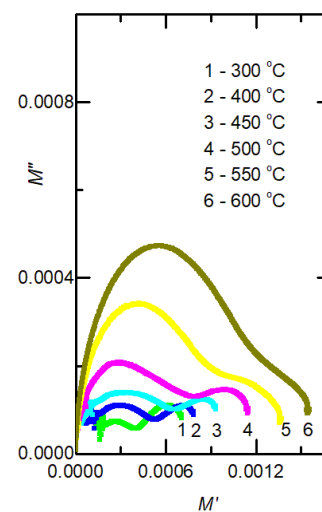

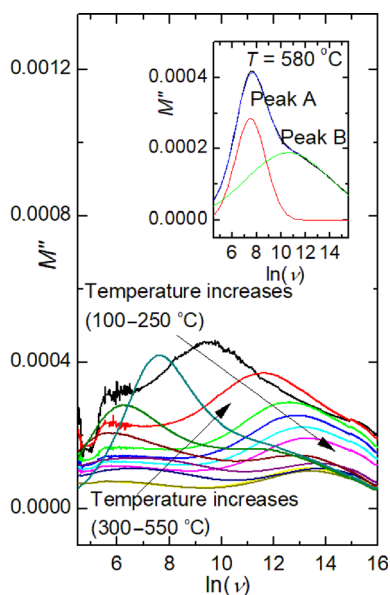**Fig. 12** Complex modulus spectra (M'' vs. M') of NBT ceramics at various temperatures.

Fig. 13 Dependences of the imaginary parts of the complex modulus *M″* of NBT ceramics on frequency. The inset shows an example of a fit for a temperature of 580 ℃.

Fig. 14 Dependence of the relaxation time of NBT ceramics, calculated from the modulus spectrum (*M″* vs. frequency) for peak A (grain boundary), on 1/*T*. The arrows show the temperatures at which crystal symmetry changes upon heating. *R*, *T*, (*R* + *T*), and *C* denote rhombohedral, tetragonal, coexisting rhombohedral and tetragonal phases, and cubic symmetry, respectively.

phenomena such as space-charge ($0–10^2$ Hz) and relaxation phenomena ($10^2–10^6$ Hz) were observed. In the low frequency range, the charge of the depletion region is affected, because oscillation is optimal. A depletion region forms between two grains. The perturbation observed in this frequency region is likely to result from an elastic clamping effect. That is the interior grain volumes by undergoing the ferroelectric transformation and thus somewhat disordered grain boundary region. Additionally, as can be seen, the spectra are broad and rather complex (see the inset in Fig. 13). In such cases, separating the contribution of the primary process from those of the secondary ones is somewhat problematic. To solve this problem, the Gaussian function was used (see the inset in Fig. 13).

The dependence of the position of the *M″* peak on frequency at various temperatures may be used to determine the most probable τ using the following equation: $\tau = 1/2\pi f$. The dependence of τ for NBT as a function of reciprocal temperature 1/*T* (K^{-1}) is shown in Fig. 14. The plot appears to be partially linear, which means that it follows the Arrhenius equation, $\tau = \tau_0 \exp(–E_a/k_B T)$, where τ_0 is the pre-exponential factor, and E_a stands for activation energy. The τ is related to a thermally activated process. The E_a values calculated from the slope of curves representing lnτ vs. 1/*T* for NBT are 1.25, 0.34, 0.10 for the grain boundaries and 0.76, 0.16, 0.46 eV for grain interiors, respectively. Thus, the E_a of grain boundaries is higher than that of
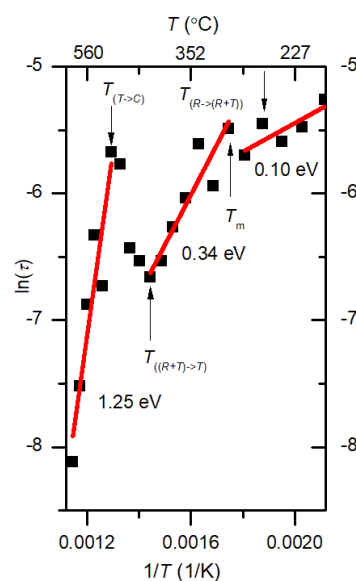
the grain interiors. This suggests a difference in the structure/composition of grain interiors and grain boundaries. The obtained values of activation energy are similar to those obtained from DC electrical conductivity measurements. The structure of NBT is a very complex system, especially considering how ions occupy the A-site position. Any non-stoichiometry that might be induced at the A-site during material processing can cause the formation of oxygen vacancies. An obvious consequence of the increased concentration of oxygen vacancies is an increase in ionic conductivity in NBT, as evidenced by the value of activation energy obtained for grain boundaries at high temperatures (1.25 eV). For bulk material and the same temperature range, the calculated E_a is 0.76 eV (values in the range from *ca.* 0.7 to 0.8 were obtained by other scientific groups [54,55]). Such electrical phenomena in the material may be modelled appropriately by means of an equivalent resistance-capacity RC electrical circuit.

4   Conclusions

A conventional solid-state method was applied to synthesize lead-free NBT ceramics. The structural test results showed rhombohedral symmetry with the space

group $R3c$. σ_{DC} and σ_{AC}, polarization and depolarization currents, I–U characteristics, and α of these ceramics were determined. Both σ_{DC} and σ_{AC} exhibited a thermally activated character and were characterized by anomalies at T_d and T_m. The activation energy of dielectric polarization was similar to the activation energy of the DC electrical conductivity.

It was found that Ohm's law satisfies the power dependence $\sigma_{AC} - \omega^s$. The s was in the range of 0–1 and decreased as a function of temperature increasing. Hopping, small polarons, and oxygen vacancies were proposed as mechanisms underlying electrical conduction for ranges of low, middle, and high temperatures, respectively.

It was shown that Ohm's law is satisfied for low voltages; for high voltages, the observed dependences are I–U^2, I–U^4, and subsequently, I–U^6.

The Seebeck coefficient measurements showed that with increasing temperature, charge carriers change the conduction type ($p \rightarrow n \rightarrow p$) and their density and mobility also change. These measurements also allowed the T_d and T_m temperatures that are specific to NBT to be distinguished.

The complex modulus, relaxation time, and activation energy were determined from impedance spectroscopic measurements. These measurements showed that as temperature rises, the grain capacity and grain boundary decrease. In addition, the determined activation energy values revealed differences in the structure/composition of grain interiors and grain boundaries. These values were similar to those determined from direct current measurements.

References

[1] Fu HX, Cohen RE. Polarization rotation mechanism for ultrahigh electromechanical response in single-crystal piezoelectrics. *Nature* 2000, **403**: 281–283.

[2] Lee MH, Kim DJ, Park JS, *et al*. High-performance lead-free piezoceramics with high curie temperatures. *Adv Mater* 2015, **27**: 6976–6982.

[3] Suchanicz J, Kluczewska K, Czaja P, *et al*. The influence of electric poling on structural, thermal, dielectric and ferroelectric properties of $Na_{0.5}Bi_{0.5}TiO_3$ ceramics. *Ceram Int* 2017, **43**: 17194–17201.

[4] Liu LJ, Yang Z, Wu MX, *et al*. Dielectric properties of $(NaBi_{(1-x)}K_x)_{0.5}Ti_{(1-x)}Nb_xO_3$ ceramics fabricated by mechanical alloying. *J Alloys Compd* 2010, **507**: 196–200.

[5] Suchanicz J, Kluczewska K, Czaja P, *et al*. Influence of sintering conditions on structural, thermal, electric and ferroelectric properties of $Na_{0.5}Bi_{0.5}TiO_3$ ceramics. *Phase Transit* 2018, **91**: 26–37.

[6] Lidjici H, Lagoun B, Berrahal M, *et al*. XRD, Raman and electrical studies on the $(1-x)(Na_{0.5}Bi_{0.5})TiO_3$–$xBaTiO_3$ lead free ceramics. *J Alloys Compd* 2015, **618**: 643–648.

[7] Suchanicz J, Mercurio JP, Konieczny K. Electric properties of $(Na_{0.5}Bi_{0.5})_{0.86}Ba_{0.14}TiO_3$ single crystal. *Ferroelectrics* 2002, **268**: 357–362.

[8] Hiruma Y, Aoyagi R, Nagata H, *et al*. Ferroelectric and piezoelectric properties of $K_{0.5}Bi_{0.5}TiO_3$ ceramics. *Jpn J Appl Phys* 2005, **44**: 5040–5044.

[9] Suchanicz J, Kania A, Czaja P, *et al*. Structural, thermal, dielectric and ferroelectric properties of $K_{0.5}Bi_{0.5}TiO_3$ ceramics. *J Eur Ceram Soc* 2018, **38**: 567–574.

[10] Liu L, Knapp M, Ehrenberg H, *et al*. The phase diagram of $K_{0.5}Bi_{0.5}TiO_3$–$Na_{0.5}Bi_{0.5}TiO_3$. *J Appl Cryst* 2016, **49**: 574–584.

[11] Suchanicz J, Faszczowy I, Sitko D, *et al*. Structural, thermal, dielectric and ferroelectric properties of $Na_{0.5}K_{0.5}NbO_3$ and $Na_{0.5}K_{0.5}NbO_3$+0.5mol%MnO_2 ceramics. *Phase Transit* 2014, **87**: 992–1001.

[12] Hu D, Pan ZB, Zhang X, *et al*. Greatly enhanced discharge energy density and efficiency of novel relaxation ferroelectric BNT–BKT-based ceramics. *J Mater Chem C* 2020, **8**: 591–601.

[13] Hu D, Pan ZB, He ZY, *et al*. Significantly improved recoverable energy density and ultrafast discharge rate of $Na_{0.5}Bi_{0.5}TiO_3$-based ceramics. *Ceram Int* 2020, **46**: 15364–15371.

[14] Ding J, Pan ZB, Chen PX, *et al*. Enhanced energy storage capability of $(1-x)Na_{0.5}Bi_{0.5}TiO_3$–$xSr_{0.7}Bi_{0.2}TiO_3$ free-lead relaxor ferroelectric thin films. *Ceram Int* 2020, **46**: 14816–14821.

[15] Jones GO, Thomas PA. Investigation of the structure and phase transitions in the novel A-site substituted distorted perovskite compound $Na_{0.5}Bi_{0.5}TiO_3$. *Acta Crystallogr Sect B* 2002, **58**: 168–178.

[16] Kusz J, Suchanicz J, Böhm H, *et al*. High temperature X-ray single crystal study of $Na_{0.5}Bi_{0.5}TiO_3$. *Phase Transit* 1999, **70**: 223–229.

[17] Suchanicz J, Kusz J, Böhm H, *et al*. Structural and electric properties of $(Na_{0.5}Bi_{0.5})_{0.88}Ba_{0.12}TiO_3$. *J Mater Sci* 2007, **42**: 7827–7831.

[18] Jones GO, Thomas PA. The tetragonal phase of $Na_{0.5}Bi_{0.5}TiO_3$—A new variant of the perovskite structure. *Acta Cryst B* 2000, **56(Pt 3)**: 426–430.

[19] Suchanicz J. Elastic constants of $Na_{0.5}Bi_{0.5}TiO_3$ single crystal. *J Mat Sci* 2002, **37**: 489–491.

[20] Suchanicz J, Lewczuk U, Konieczny K. Effect of Ba doping on the structural, dielectric and ferroelectric properties of $Na_{0.5}Bi_{0.5}TiO_3$ ceramics. *Ferroelectrics* 2016, **497**: 85–91.

[21] Trolliard G, Dorcet V. Reinvestigation of phase transitions in $Na_{0.5}Bi_{0.5}TiO_3$ by TEM. Part II: Second order orthorhombic to tetragonal phase transition. *Chem Mater* 2008, **20**: 5074–5082.

[22] Vakhrushev SB, Isupov VA, Kvyatkovsky BE, *et al*. Phase transitions and soft modes in sodium bismuth titanate. *Ferroelectrics* 1985, **63**: 153–160.

[23] Barick BK, Mishra KK, Arora AK, *et al*. Impedance and Raman spectroscopic studies of $Na_{0.5}Bi_{0.5}TiO_3$. *J Phys D:*

Appl Phys 2011, **44**: 355402.

[24] East J, Sinclair DC. Characterization of $(Bi_{1/2}Na_{1/2})TiO_3$ using electric modulus spectroscopy. *J Mater Sci Lett* 1997, **16**: 422–435.

[25] Saradhi BVB, Srinivas K, Prasad G, Suryanarayana SV, Bhimasankaram T. Impedance spectroscopic studies in ferroelectric $Na_{0.5}Bi_{0.5}TiO_3$. *Mat Sci Eng B* 2003, **98**: 10–16.

[26] Karpierz M, Suchanicz J, Konieczny K, *et al*. Effects of $PbTiO_3$ doping on electric properties of $Na_{0.5}Bi_{0.5}TiO_3$ ceramics. *Phase Transit* 2017, **90**: 65–71.

[27] Petzelt J, Nuzhnyy D, Bovtun V, *et al*. Peculiar Bi-ion dynamics in $Na_{0.5}Bi_{0.5}TiO_3$ from terahertz and microwave dielectric spectroscopy. *Phase Transiti* 2014, **87**: 953–965.

[28] Rao BN, Ranjan R. Electric-field-driven monoclinic-to-rhombohedral transformation in $Na_{0.5}Bi_{0.5}TiO_3$. *Phys Rev B* 2012, **86**: 134103.

[29] Jain Ruth DE, Sundarakannan B. Structural and Raman spectroscopic studies of poled lead-free piezoelectric sodium bismuth titanate ceramics. *Ceram Int* 2016, **42**: 4475–4478.

[30] Information on http://www.icdd.com/pdfsearch.

[31] Scott JF, Araujo CA, Melnick BM, *et al*. Quantitative measurement of space-charge effects in lead zirconate-titanate memories. *J Appl Phys* 1991, **70**: 382–388.

[32] Kluczewska K, Sitko D, Suchanicz J, *et al*. Isothermal depolarization currents of $Na_{0.5}Bi_{0.5}TiO_3$ ceramics. *Phase Transit* 2018, **91**: 1060–1066.

[33] Grekov AA, Korchagina NA, Rogach ED, *et al*. Slow relaxation processes in SbSI crystals. *Ferroelectrics* 1982, **45**: 71–75.

[34] Wieder HH. Retarded polarization phenomena in $BaTiO_3$ crystals. *J Appl Phys* 1956, **27**: 413–416.

[35] Kao KC, Hwang W. *Electrical Transport in Solids*. Oxford (UK): Pergamon Press, 1981.

[36] Wang CC, Lei CM, Wang GJ, *et al*. Oxygen-vacancy-related dielectric relaxations in $SrTiO_3$ at high temperatures. *J Appl Phys* 2013, **113**: 094103.

[37] Selvamani R, Singh G, Tiwari VS, *et al*. Oxygen vacancy related relaxation and conduction behavior in $(1–x)$ NBT–xBiCrO_3 solid solution. *Phys Stat Sol (a)* 2012, **209**: 118–125.

[38] Li LH, Li M, Zhang HR, *et al*. Controlling mixed conductivity in $Na_{1/2}Bi_{1/2}TiO_3$ using A-site non-stoichiometry and Nb-donor doping. *J Mater Chem C* 2016, **4**: 5779–5786.

[39] Joncher AK. *Dielectric Relaxation in Solids*. London (UK): Chelsea Dielectric Press Ltd, 1983.

[40] Cox TA. *Transition Metal Oxides*. Oxford (UK): Oxford University Press, 1992.

[41] Austin IG, Mott NF. Polarons in crystalline and non-crystalline materials. *Adv Phys* 1969, **18**: 41–102.

[42] Botter H, Bryksin VV. *Hopping Conduction in Solids*. Berlin (Germany): Akademie Verlag, 1985.

[43] Sharma GD, Roy M, Roy MS. Charge conduction mechanism and photovoltaic properties of 1,2-diazoamino diphenyl ethane (DDE) based Schottky device. *Mater Sci Eng: B* 2003, **104**: 15–25.

[44] Salam R. Trapping parameters of electronic defectes states in indium tin oxide from AC conductivity. *Phys Stat Sol (a)* 1990, **117**: 535–540.

[45] Saha S, Krupanidhi SB. Dielectric response in pulsed laser ablated $(Ba,Sr)TiO_3$ thin films. *J Appl Phys* 2000, **87**: 849–854.

[46] Rose A. Space-charge-limited currents in solids. *Phys Rev* 1955, **97**: 1538.

[47] Lampert MA. Simplified theory of space-charge-limited currents in an insulator with traps. *Phys Rev* 1956, **103**: 1648.

[48] Huey RM, Taylor RM. Anomalous discharges in ferroelectrics. *J Appl Phys* 1963, **34**: 1557–1560.

[49] Grushevski YA, Sleptsov AI. Electronic polarization in SbSI near electrodes. *Izv VUZ FIZ* 1969, **12**: 1546–1549.

[50] Burgienko VI. ELectron traps in silver chloride crystals. *Izv VUZ FIZ* 1965, **8**: 64–66.

[51] Breckenridge RG, Hosler WR. Electrical properties of titanium dioxide semiconductors. *Phys Rev* 1953, **91**: 793–802.

[52] Macedo PB, Moynihan CT, Bose R. Role of ionic diffusion in polarization in vitreous ionic conductors. *Phys Chem Glasses* 1972, **13**: 171–179.

[53] Angell CA. Dynamic processes in ionic glasses. *Chem Rev* 1990, **90**: 523–542.

[54] Li M, Pietrowski MJ, De Souza RA, *et al*. A family of oxide ion conductors based on the ferroelectric perovskite $Na_{0.5}Bi_{0.5}TiO_3$. *Nat Mater* 2014, **13**: 31–35.

[55] Schütz D, Deluca M, Krauss W, *et al*. Lone-pair-induced covalency as the cause of temperature- and field-induced instabilities in bismuth sodium titanate. *Adv Funct Mater* 2012, **22**: 2285–2294.